

Investigation of magnetic excitations and charge order in a van der Waals ferromagnet Fe_5GeTe_2

V. K. Bhartiya,^{1,*} T. Kim,¹ J. Li,¹ T. P. Darlington,² D. J. Rizzo,²
Y. Gu,¹ S. Fan,¹ C. Nelson,¹ J. W. Freeland,³ X. Xu,⁴ D. N.
Basov,² J. Pelliciari,¹ A. F. May,⁵ C. Mazzoli,¹ and V. Bisogni^{1,†}

¹*National Synchrotron Light Source II, Brookhaven
National Laboratory, Upton, New York 11973, USA.*

²*Department of Physics, Columbia University, New York, New York 10027, USA.*

³*Advanced Photon Source, Argonne National Laboratory, Lemont, IL, USA.*

⁴*Department of Physics, University of Washington, Seattle, Washington 98195, USA.*

⁵*Materials Science and Technology Division,
Oak Ridge National Laboratory, Oak Ridge, Tennessee 37831, USA.*

(Dated: November 22, 2024)

Understanding the complex ground state of van der Waals (vdW) magnets is essential for designing new materials and devices that leverage these platforms. Here, we investigate a two-dimensional vdW ferromagnet – Fe_5GeTe_2 – with one of the highest reported Curie temperatures, to elucidate its magnetic excitations and charge order. Using Fe L_3 –edge resonant inelastic x-ray scattering, we find the dual character of magnetic excitations, consisting of a coherent magnon and a continuum, similar to what is reported for its sister compound Fe_3GeTe_2 . The magnon has an energy of ≈ 36 meV at the maximum in-plane momentum transfer (-0.35 r.l.u.) allowed at Fe L_3 –edge. A broad and non-dispersive continuum extends up to 150 meV, 50% higher energy than in Fe_3GeTe_2 . Its intensity is sinusoidally modulated along the L direction, with a period matching the inter-slab distance. Our findings suggest that while the unconventional dual character of magnetic excitations is generic to ternary Fe-Ge-Te vdW magnets, the correlation length of the out-of-plane magnetic interaction increases in Fe_5GeTe_2 as compared to Fe_3GeTe_2 , supporting a stronger three-dimensional character for the former. Furthermore, by investigating the $\pm(1/3, 1/3, L)$ peaks by resonant x-ray diffraction, we conclude these to have structural origin rather than charge order – as previously reported – and suggest doubling of the structural unit cell along the c –axis.

The discovery of ferromagnetism in two-dimensional van der Waals ferromagnets have opened exciting frontiers in quantum matter research [1–3]. In this context, the ternary Fe-Ge-Te vdW materials, such as Fe_3GeTe_2 and Fe_5GeTe_2 , hosting high-temperature long-range ferromagnetic order down to the two-dimensional (2D) structural limit is a unique platform where miniaturized spintronics devices have already been proposed [4–14]. In addition, strong electronic correlations are reported to drive these systems towards exotic ground states, that is, the heavy Fermions/ Kondo physics [15, 16], charge order (CO) [17], and orbital selective Mott transitions (OSMT) [18].

Fe_3GeTe_2 ($150 < T_C < 230$ K) is the most thoroughly investigated member of the ternary

* vbhartiya1@bnl.gov

† bisogni@bnl.gov

Fe-Ge-Te vdW magnets. One of the intriguing findings is the coexistence of low energy coherent magnetic excitations (magnons) and a dispersionless non-Stoner type continuum at higher energies [16, 18, 19]. This dual character of magnetic excitations is beyond the framework of the linear spin wave theory, invoking the OSMT scenario – atypical to $3d$ transition metals – to explain the experimental observations [18]. Are these dual magnetic excitations, a generic feature of the ternary Fe-Ge-Te vdW materials? If so, how these excitations evolve with T_C ?

Fe_5GeTe_2 with the highest $T_C \approx 315$ K among Fe-Ge-Te 2D-vdW ferromagnetic materials is an ideal member to investigate these questions. Moreover, it hosts the long-range ferromagnetic order remarkably close to room temperature ≈ 270 K in the 2D structural limit [4–6, 8]. Deciphering the mechanism behind these high temperature 2D vdW ferromagnets is essential to engineer novel heterostructures from 2D layers. However, despite enormous progress in understanding transport, magnetic and structural properties of Fe_5GeTe_2 [4–6], to date, the character of the magnetic excitations, their energy scale, and dimensionality remain unexplored in this material. Inelastic neutron scattering (INS) is a standard technique to address these issues [20, 21] but the small size of the Fe_5GeTe_2 single crystals poses a challenge. Furthermore, a recent angular resolved photoemission spectroscopy (ARPES) and scanning tunneling microscopy (STM) study reports a charge order [17], that is shown to compete with the magnetic ordering. However, a bulk-sensitive signature of the CO, its electronic character and propagation vector are unexplored so far.

Here we present an investigation of the magnetic excitations and charge order in Fe_5GeTe_2 . To elucidate the character, energy scale, and dimensionality of the magnetic excitations, we employed high-resolution Fe L_3 -edge resonant inelastic x-ray scattering (RIXS) on a mm sized single crystal Fe_5GeTe_2 . RIXS complements INS to probe collective spin excitations and, in addition, can measure small sample volumes [22] easily accessing the high-energy spectral range where the thermal neutron flux is heavily reduced. Our findings suggests that Fe_5GeTe_2 hosts dual character of magnetic excitations, similarly to Fe_3GeTe_2 , and despite being a 2D system structurally, it displays a significant three-dimensional (3D) interaction between Fe-Ge-Te slabs that are ~ 10 Å apart. To investigate the bulk and electronic character of the proposed CO, we used x-ray diffraction (XRD) and Fe K -edge resonant elastic x-ray scattering (REXS) [23–25]. Our results demonstrate that the observed $\pm(1/3, 1/3, L)$ peaks are of structural origin, suggesting a doubling of structural unit

cell along the c -axis. Overall, our work advances the current understanding of the magnetic properties of Fe_5GeTe_2 and shed light onto the whole family of Fe-Ge-Te vdW magnets.

1. SAMPLE AND EXPERIMENTAL DETAILS

The high quality quenched single crystal of $\text{Fe}_{4.75}\text{GeTe}_2$ used for this study was taken from the same batch as in Ref. [4, 26]. For simplicity, we refer to $\text{Fe}_{4.75}\text{GeTe}_2$ as Fe_5GeTe_2 throughout the text. Figure 1(a) shows the rhombohedral unit cell of Fe_5GeTe_2 ($R\bar{3}m$ No. 166, $a = b \sim 4.04 \text{ \AA}$, $c \sim 29.19 \text{ \AA}$), characterized by three distinct Fe-Ge-Te slabs separated by $\sim 11 \text{ \AA}$. Within each slab, the Fe and Ge atoms occupy interior positions, while the Te atoms occupy the external positions. Fe_5GeTe_2 develops ferromagnetic order below $T_C \sim 315 \text{ K}$ with magnetic moment pointing along the c -axis [4].

For the x-ray absorption spectroscopy (XAS) and RIXS studies, the Fe_5GeTe_2 single crystal was oriented with $(1\ 0\ 0)$ and $(0\ 0\ 1)$ in the scattering plane, see Fig. 1(b). The sample was cleaved in air with scotch tape just before loading it into the vacuum chamber. Figure 1(c) shows the XAS measured in the total electron yield (TEY) mode at 70 K. The observed L_3 and L_2 absorption peaks are in agreement with literature [27], supporting the high quality of the sample. The XAS data was used to identify the resonant energy for the RIXS study. To reduce the elastic scattering signal in the RIXS measurements, we used π polarized incoming x-rays. The same sample was used for both REXS and XRD experiments, and it was aligned using an out-of-plane and two in-plane nuclear reflections.

The momentum transfer $\mathbf{Q}(HKL)$ associated with the RIXS spectra and the diffraction data are expressed in reciprocal lattice units $(4\pi/\sqrt{3}a\ 4\pi/\sqrt{3}a\ 2\pi/c)$. The in-plane and out-of-plane momentum coverage was achieved by rotating both the scattering angle Ω and the x-rays incident angle θ . Extensive momentum coverage was achieved for the XRD experiment (2 keV of photon energy) and for the Fe K -edge REXS ($\sim 7 \text{ keV}$ of photon energy). For Fe L_3 -edge RIXS ($\sim 710 \text{ eV}$ of photon energy), we could span a large portion of the \mathbf{Q} -space in the L direction across several brillouin zone (BZ) and up to $L = 3.23$ ($2\pi/c$), thanks to the large c -axis ($\sim 29.19 \text{ \AA}$) of the Fe_5GeTe_2 , while in-plane we could cover up to $H_{max} = -0.35$ ($4\pi/\sqrt{3}a$) within the first BZ.

2. RESULTS AND DISCUSSION

2.1. Magnetic excitations in Fe_5GeTe_2

In the following two sections we describe the investigation of the magnetic excitations and their momentum dependence in Fe_5GeTe_2 using Fe L_3 -edge RIXS, and we discuss the results in comparison Fe_3GeTe_2 [16, 18, 28]. Figure 1(d) presents a RIXS intensity map measured as a function of incident photon energy across the Fe L_3 -edge. Although most of the spectral weight goes into high-energy fluorescence as expected for a metal (see Supplementary Fig. S3.1) [22], a weak component stretches from 0 up to ~ 150 meV resonating at the Fe L_3 peak.

By fixing the incident photon energy to the maximum of the Fe L_3 resonance, we measured high-resolution RIXS spectra as a function of momentum transfer \mathbf{Q} .

Figures 1(e,f) show RIXS spectra at two representative \mathbf{Q} points with largest in-plane momentum components, $\mathbf{Q} = (-0.35 \ 0 \ 1.4)$ and $(-0.3 \ 0 \ 1.74)$. We make use of both RIXS spectra to establish a minimum fitting model that describes the observed inelastic spectral weight below 200 meV. Details regarding the fitting and its procedure are reported in Supplementary Note S3. Taking Fe_3GeTe_2 as a reference case [16, 18], we include in the fitting model a resolution limited phonon (blue peak), a magnon mode (red peak) due to spin-spin correlations between localized spins, and a broad magnetic continuum (green peak) coming from spin-spin interactions among itinerant electrons. We fix the phonon energy to 20 meV based on the room temperature Raman measurements presented in Supplementary Fig. S1.1 and consistently with [18]. From the remaining spectral weight, we extract a magnon peak centered at $36 \text{ meV} \pm 1 \text{ meV}$ and a continuum centered at $75 \text{ meV} \pm 2 \text{ meV}$, extending up to ~ 150 meV. At higher energies, a background from the fluorescence tail dominates the spectral weight (gray solid line).

For the spectra presented in Figs. 1(e,f), we were not able to resolve any significant magnon dispersion given the proximity of the in-plane \mathbf{Q} components. However, a comparable magnon energy for similar momentum transfer has been reported for Fe_3GeTe_2 [16, 18, 28], further supporting the nature of the ~ 36 meV peak. Similarly, the broad continuum peak (stretching up to 150 meV) resembles the one identified in Fe_3GeTe_2 [16], although in the latter system it extends only up to 100 meV. Based on these findings, we

identify the low energy magnetic excitations in Fe_5GeTe_2 , and we confirm the coexistence of the dual electron spin character - localized and itinerant - similarly to Fe_3GeTe_2 . This result suggests that OSMT scenario should be considered also for Fe_5GeTe_2 .

2.2. Origin of the magnetic continuum

Figure 2 shows the L dependent RIXS spectra along $(0\ 0\ L)$ from $L = 1.74$ r.l.u. to $L = 3.23$ r.l.u. In these measurements, we maximized the out-of-plane coverage by scanning mostly along $(0\ 0\ L)$, while minimizing the in-plane momentum transfer, e.g. $H < |0.04|$ r.l.u. and $K = 0$ r.l.u. A clear continuum peak emerges from all spectra, see Figs. 2 (a-g), and its position remains mostly invariant versus L as marked by a vertical dashed line. The dispersionless nature of the continuum agrees with the Fe_3GeTe_2 findings [16]. To directly compare the absolute RIXS intensities as a function of L (or scattering geometries), all spectra reported here are self-absorption corrected as described in Supplementary Note S2. Already from the raw data, the continuum intensity appears to decrease for decreasing L . Note that while in Fe_3GeTe_2 the continuum is maximized around the in-plane BZ boundary [16], here we find a significant spectral weight close to the in-plane BZ center.

The origin of the L -dependent intensity modulation of the continuum in Fe_3GeTe_2 was associated with the two Fe sites, yielding a characteristic length scale along the c -axis within Fe-Ge-Te slab [16]. The goal of this section is to extract this information for Fe_5GeTe_2 . We fit the RIXS spectra in Fig. 2 using the model introduced in Figs. 1(e,f). To effectively implement the fitting model, we made some key assumptions. Given the strong elastic line intensity and the unknown magnon dispersion for this material, we fixed the fitting parameters (peak position and width) of the lowest energy modes - phonon and magnon - to match the values extracted for $\mathbf{Q} = (-0.35\ 0\ 1.4)$ r.l.u. In this way, we could account for most of the low energy spectral weight (below 40 meV), without affecting the dispersionless continuum. Regarding the fitting of the continuum itself, we fixed its position and width to reproduce the broad and dispersionless character of this excitation [16, 18], while its amplitude was allowed to change. More details on the fitting procedure can be found in Supplementary Note S3. As a result of this analysis, we obtain the L -dependent evolution of the continuum intensity which follows a sinusoidal behavior, as highlighted in Fig. 2 (h).

When dealing with a continuum or a dispersionless excitation, the \mathbf{Q} -dependent modula-

tion of its intensity or structure factor encodes the distance between the interacting atoms along the selected \mathbf{Q} -direction. Hard x-ray RIXS and INS – enabling a wide coverage of reciprocal space – have been extensively used to show the formation of new magnetic superstructures by monitoring the \mathbf{Q} -modulation of the spectral weight [16, 29, 30]. Following these works, the frequency of the continuum structure factor modulation can be captured by a simple qualitative function:

$$I(L) \propto \cos(L \cdot d/2)^2, \quad (1)$$

where L is the momentum transfer vector and d is the real space inter-atomic distance along the c -axis within the unit cell. By fitting the data points displayed in Fig. 2 (h), we extract a distance of $d = 10 \pm 1 \text{ \AA}$.

In the case of Fe_3GeTe_2 , the L -dependent INS structure factor of the continuum yielded an intra-slab distance $d \sim 2.7 \text{ \AA}$ [16]. Such a length-scale corresponds to the Fe-Fe dumbbell (a dimer like structure corresponding to the largest exchange interaction) superstructure oriented along the c -axis within an individual Fe-Ge-Te slab. This finding suggests that the magnetic continuum in Fe_3GeTe_2 originates from the quasi-molecular character of the magnetic states formed by the Fe-Fe dumbbell, and furthermore it identifies the atoms and exchange path that contribute to the strongest magnetic exchange interaction in the system [18].

To identify the interacting atoms and exchange path behind the continuum intensity modulation in Fe_5GeTe_2 , we display in Fig. 2 (i) a simulation of $I(L)$ based on a representative intra-slab distance (red), and inter-slab distance (black). Such distances are highlighted in the unit cell of Fig. 2 (l), using the same color code. The intra-slab distance $d \sim 2.53 \text{ \AA}$ connecting two Fe atoms within the same Fe-Ge-Te slab fails in reproducing the observed modulation, despite it well described the L -dependent continuum modulation for Fe_3GeTe_2 [16]. Rather, we find that an inter-slab distance $d \sim 11 \text{ \AA}$ connecting the center of two consecutive slabs well reproduces the continuum modulation for Fe_5GeTe_2 . Our finding supports the presence of an inter-slab exchange path along the c -axis, suggesting a three-dimensional character for the magnetic interaction in Fe_5GeTe_2 . Additionally, we identify the Fe-Ge-Te slabs as the interacting magnetic units in Fe_5GeTe_2 . This is consistent with recent x-ray magnetic circular dichroism (XMCD) and ARPES studies underlining the key role of Te and Ge in determining the itinerant long-range ferromagnetism in Fe_5GeTe_2 [27, 31], owing to

the strong hybridization and covalent nature of the Fe-Te and the Fe-Ge bonds. Based on atomic position considerations, we suggest that the shorter Fe-Te nearest neighbor distance (2.63 Å) in Fe_5GeTe_2 with respect to Fe_3GeTe_2 (2.643 Å) possibly favors the inter-slab exchange mediated by the Te sites (highlighted by the curved line in Fig. 2(j)). Overall, we speculate that the inter-slab exchange interaction revealed by our study could be crucial for determining the high T_C in Fe_5GeTe_2 , endorsed by recent studies on epitaxially grown thin films where T_C is found to be inversely proportional to the inter-slab distance [32].

2.3. Absence of charge order in bulk Fe_5GeTe_2

Recently, selected area electron diffraction studies [33] reported a superstructure modulation vector $\mathbf{Q}_1 = \pm 1/3 (1\ 1\ 3)$ above 100 K, fading away at lower temperatures with a diffused line along $1/3 (1\ 1\ L)$ together with a new $\mathbf{Q}_2 = \pm 3/10 (0\ 0\ 3L)$ order. A short range $\sqrt{3}a \times \sqrt{3}a R30^\circ$ order was observed by single crystal XRD and the high-angle annular dark field image and associated with Fe occupancy of a crystallographic split-site [4]. Further STM and ARPES investigations [17] confirmed the existence of a $\sqrt{3}a \times \sqrt{3}a R30^\circ$ in-plane periodic modulation and assigned it to charge ordering. To further the understanding of the bulk signature, electronic character and propagation vectors of \mathbf{Q}_1 and \mathbf{Q}_2 in Fe_5GeTe_2 , we present synchrotron XRD (~ 2.1 keV) and REXS (Fe K -edge, ~ 7.1 keV) investigations.

We confirmed the in-plane order $\sqrt{3}a \times \sqrt{3}a R30^\circ$ in our Fe_5GeTe_2 single crystal by finding several symmetry-equivalent peaks at 150 K, as represented in Fig. 3(a). Figure 3(b) reports the H , K , and L scans of a representative peak with $(1/3\ 1/3)$ in-plane components, measured using ~ 2.1 keV x-rays. Interestingly, we find that the out-of-plane component peaks at $L = 7.5$ r.l.u. No significant temperature dependence is detected for this peak while going across 100 K, as displayed in Fig. 3(c). The extended L scan of $(2/3\ -1/3\ L)$ and $(1/3\ 1/3\ L)$ peaks are presented in Fig. 3(d), using ~ 7.1 keV x-rays (dotted lines): a clear $(1/3\ 1/3\ 3n+1.5)$ with $n = 0, 1, 2, 3, \dots$ periodicity emerges even at 7 K. The observed $(1/3\ 1/3\ 3n+1.5)$ modulation differs from the previously reported $\pm 1/3 (1\ 1\ 3)$ order [33] and it is also distinct from the $(0\ 0\ 3n)$ selection rule expected for a rhombohedral unit cell (space group $R\bar{3}m$). For reference, we reproduce in Fig. 3(d) the $(0\ 0\ L)$ scan (gray line) showing the $(0\ 0\ 3n)$ periodicity of the structural Bragg peak. The satellite structure visible in the $(0\ 0\ L)$ scan is attributed to a second crystallite present in the sample. Also no fingerprint

of $\mathbf{Q}_2 = \pm 3/10(0\ 0\ 3L)$ is observed in our data down to 7 K.

The intensities of $(0\ 0\ L)$ and $(2/3\ -1/3\ L)$ or $(1/3\ 1/3\ L)$ scans cannot be directly compared in Fig. 3(d), as we used a higher intensity detuning filter for the main structural Bragg peaks along $(0\ 0\ L)$. An absolute intensity comparison between $(1/3\ 1/3\ 22.5)$ and $(0\ 0\ 9)$ is presented in 3(d), showing that the intensities of both peaks are of the same order of magnitude, with the $(0\ 0\ 9)$ peak approximately 50% stronger than $(1/3\ 1/3\ 22.5)$.

Additionally, using Fe K -edge REXS, we investigated the resonance effect of the $(1/3\ 1/3\ 22.5)$ peak. The resulting fixed- \mathbf{Q} energy scan is presented in Fig. 3(e) (green dotted line), and compared to the energy scan of the $(0\ 0\ 9)$ structural Bragg peak (gray line). Both scans present a similar behavior, with no resonance enhancement. The Fe K -edge XAS of Fe_5GeTe_2 is reproduced for reference in the same figure.

Overall, our REXS and XRD studies report the presence of a commensurate $(1/3\ 1/3\ L)$ Bragg peak with a $3n+1.5$ out-of-plane modulation, no temperature dependence down to 7 K, and no resonance effect. Based on these observations, we propose these peaks to be of structural origin rather than electronic [23–25, 34]. This conclusion is further corroborated by the comparable peak intensity with respect to main structural Bragg peaks. Furthermore, we underline that the observed $3n+1.5$ out-of-plane periodicity is not compatible with the space group $R\bar{3}m$ proposed for Fe_5GeTe_2 , instead, it infers doubling of structural unit cell along the \mathbf{c} -axis.

To reconcile the discrepancy between our observations and the ones reported in the literature [17, 33], we should acknowledge intrinsic differences connected with the techniques involved. STM and ARPES mostly probe the surface, which in certain materials can significantly differ from the bulk [35–38]. Electron diffraction instead probes the bulk, but the required sample preparation methods - such as focused ion beam and grinding - might introduce permanent micro-structural changes affecting the material response [39, 40]. Finally, we cannot exclude a sample to sample variation in determining the ultimate material properties. Fe_5GeTe_2 single crystals are known to have stacking faults and different samples (especially grown by different groups) might even have slightly different Fe concentration.

3. CONCLUSION AND OUTLOOK

Our work sheds light on the magnetic excitations and electronic order in the room temperature vdW ferromagnet Fe_5GeTe_2 . Using high-resolution RIXS at the Fe L_3 -edge, we reveal that Fe_5GeTe_2 hosts dual character of magnetic excitations composed of a magnon and a continuum, similarly to the more extensively characterized Fe_3GeTe_2 , and prove that the dual character of magnetic excitation driven by orbital-selective Mott transition is common to ternary Fe-Ge-Te vdW materials. The out-of-plane modulation of the continuum intensity reveals the presence of a strong out-of-plane inter-slab exchange path, where the interacting magnetic units are the neighboring Fe-Ge-Te slabs. We conclude that Fe_5GeTe_2 behaves like a 3D magnet, and we discuss this finding in connection to its T_C , the highest among Fe-Ge-Te vdW materials. Additionally, employing XRD and REXS, we explored the bulk character, the electronic origin and the propagation vector of the previously reported charge order with $(1/3\ 1/3)$ in-plane components. The absence of temperature and resonance effects, and the commensurability with the crystal structure lead us to conclude a structural origin for the observed Bragg peaks. The identified $\pm(1/3\ 1/3\ 1.5)$ propagation vector requires doubling of the crystallographic unit cell.

ACKNOWLEDGMENTS

This work was supported as part of Programmable Quantum Materials, an Energy Frontier Research Center funded by the US Department of Energy (DOE), Office of Science, Basic Energy Sciences (BES), under award DE-SC0019443. Development of Fe_5GeTe_2 crystals (AFM) was supported by the U. S. Department of Energy, Office of Science, Basic Energy Sciences, Materials Sciences and Engineering Division. This research used beamlines 2-ID and 4-ID of NSLS-II, a US DOE Office of Science User Facility operated for the DOE Office of Science by Brookhaven National Laboratory under contract no. DE-SC0012704. This research used resources of the Advanced Photon Source, a U.S. Department of Energy (DOE) Office of Science user facility operated for the DOE Office of Science by Argonne National Laboratory under Contract No. DE-AC02-06CH11357.

AUTHOR CONTRIBUTIONS

VBi, VBh, CM, AM, DB, and XX conceived the research plan. AFM grew and characterized the bulk single crystalline Fe_5GeTe_2 . VBi, VBh, TK, JL, YG, SF, JP carried out the RIXS measurements. VBh, TK, CM, CN, JF performed the XRD and REXS experiments. TD and DJR realized the Raman measurements. VBh and VBi analyzed and interpreted the data, with contributions from all coauthors. VBh and VBi wrote the manuscript. All authors commented on the text.

METHODS

X-ray Absorption (XAS) and resonant inelastic x-ray Scattering (RIXS)

High-resolution XAS and RIXS experiments were carried out at the SIX 2-ID beamline of NSLS-II [41]. The experimental energy resolution at the Fe L_3 -edge (~ 708 eV) was 21 meV for the RIXS measurements, determined by the full width at half-maximum of the elastic peak measured from a reference multilayer sample. To suppress the elastic line, π -polarization was used throughout the experiment.

Resonant elastic x-ray scattering (REXS) and x-ray diffraction (XRD)

Synchrotron based XRD was used to measure the rocking curves and temperature dependence of $(1/3\ 1/3\ 7.5)$ peak at 29-ID beamline of APS, with a photon energy of 2.1keV. The Fe K -edge REXS was performed at the 4-ID beamline of NSLS-II.

Raman Spectroscopy

The Raman measurements were taken using a LabRAM HR Evolution Raman microscope from Horiba Scientific using $100 \times 0.9\text{NA}$ Olympus air objective. Spectra were recorded

using an 1800 gr/mm holographic grating and Synapse II front-illuminated EMCCD.

- [1] K. S. Burch, D. Mandrus, and J. G. Park, Magnetism in two-dimensional van der Waals materials, *Nature* **563**, 47 (2018).
- [2] M. Gibertini, M. Koperski, A. F. Morpurgo, and K. S. Novoselov, Magnetic 2D materials and heterostructures, *Nature Nanotechnology* **14**, 408 (2019).
- [3] Q. H. Wang, A. Bedoya-Pinto, M. Blei, A. H. Dismukes, A. Hamo, S. Jenkins, M. Koperski, Y. Liu, Q. C. Sun, E. J. Telford, H. H. Kim, M. Augustin, U. Vool, J. X. Yin, L. H. Li, A. Falin, C. R. Dean, F. Casanova, R. F. Evans, M. Chshiev, A. Mishchenko, C. Petrovic, R. He, L. Zhao, A. W. Tsen, B. D. Gerardot, M. Brotons-Gisbert, Z. Guguchia, X. Roy, S. Tongay, Z. Wang, M. Z. Hasan, J. Wrachtrup, A. Yacoby, A. Fert, S. Parkin, K. S. Novoselov, P. Dai, L. Balicas, and E. J. Santos, The Magnetic Genome of Two-Dimensional van der Waals Materials, *ACS Nano* **17**, 47 (2021).
- [4] A. F. May, D. Ovchinnikov, Q. Zheng, R. Hermann, S. Calder, B. Huang, Z. Fei, Y. Liu, X. Xu, and M. A. McGuire, Ferromagnetism near room temperature in the cleavable van der waals crystal Fe_5GeTe_2 , *ACS Nano* **13**, 57 (2019).
- [5] H. Zhang, R. Chen, K. Zhai, X. Chen, L. Caretta, X. Huang, R. V. Chopdekar, J. Cao, J. Sun, J. Yao, R. Birgeneau, and R. Ramesh, Itinerant ferromagnetism in van der Waals $\text{Fe}_{5-x}\text{GeTe}_2$ crystals above room temperature, *Phys. Rev. B* **102**, 64417 (2020).
- [6] H. Chen, S. Asif, K. Dolui, Y. Wang, J. Támara-Isaza, V. M. L. D. P. Goli, M. Whalen, X. Wang, Z. Chen, H. Zhang, K. Liu, D. Jariwala, M. B. Jungfleisch, C. Chakraborty, A. F. May, M. A. McGuire, B. K. Nikolic, J. Q. Xiao, and M. J. H. Ku, Above-room-temperature ferromagnetism in thin van der waals flakes of cobalt-substituted Fe_5GeTe_2 , *ACS Applied Materials & Interfaces* **15**, 3287 (2023).
- [7] Z. Wang, D. Sapkota, T. Taniguchi, K. Watanabe, D. Mandrus, and A. F. Morpurgo, Tunneling spin valves based on Fe_3GeTe_2 /hBN/ Fe_3GeTe_2 van der waals heterostructures, *Nano Letters* **18**, 4303 (2018).
- [8] E. Georgopoulou-Kotsaki, P. Pappas, A. Lintzeris, P. Tsipas, S. Fragkos, A. Markou, C. Felser, E. Longo, M. Fanciulli, R. Mantovan, F. Mahfouzi, N. Kioussis, and A. Dimoulas, Significant enhancement of ferromagnetism above room temperature in epitaxial 2d van der waals ferro-

- magnet $\text{Fe}_{5-\delta}\text{GeTe}_2/\text{Bi}_2\text{Te}_3$ heterostructures, *Nanoscale* **15**, 2223 (2023).
- [9] Q. Li, M. Yang, C. Gong, R. V. Chopdekar, A. T. N'diaye, J. Turner, G. Chen, A. Scholl, P. Shafer, E. Arenholz, A. K. Schmid, S. Wang, K. Liu, N. Gao, A. S. Admasu, S.-W. Cheong, C. Hwang, J. Li, F. Wang, X. Zhang, and Z. Qiu, Patterning-induced ferromagnetism of Fe_3GeTe_2 van der waals materials beyond room temperature, *Nano Lett* **18**, 7 (2018).
- [10] M. Alghamdi, M. Lohmann, J. Li, P. R. Jothi, Q. Shao, M. Aldosary, T. Su, B. P. T. Fokwa, and J. Shi, Highly efficient spin-orbit torque and switching of layered ferromagnet Fe_3GeTe_2 , *Nano Lett* **19**, 25 (2019).
- [11] M. Yang, Q. Li, R. V. Chopdekar, C. Stan, S. Cabrini, J. W. Choi, S. Wang, T. Wang, N. Gao, A. Scholl, N. Tamura, C. Hwang, F. Wang, and Z. Qiu, Highly enhanced curie temperature in ga-implanted Fe_3GeTe_2 van der waals material, *Advanced Quantum Technologies* **3** (2020).
- [12] B. Ding, Z. Li, G. Xu, H. Li, Z. Hou, E. Liu, X. Xi, F. Xu, Y. Yao, and W. Wang, Observation of magnetic skyrmion bubbles in a van der waals ferromagnet Fe_3GeTe_2 , *Nano Lett* **20**, 2023 (2020).
- [13] Y. Wu, S. Zhang, J. Zhang, W. Wang, Y. L. Zhu, J. Hu, G. Yin, K. Wong, C. Fang, C. Wan, X. Han, Q. Shao, T. Taniguchi, K. Watanabe, J. Zang, Z. Mao, X. Zhang, and K. L. Wang, Néel-type skyrmion in $\text{WTe}_2/\text{Fe}_3\text{GeTe}_2$ van der Waals heterostructure, *Nature Communications* **2020 11:1** **11**, 1 (2020).
- [14] Y. Deng, Y. Yu, Y. Song, J. Zhang, N. Z. Wang, Z. Sun, Y. Yi, Y. Z. Wu, S. Wu, J. Zhu, J. Wang, X. H. Chen, and Y. Zhang, Gate-tunable room-temperature ferromagnetism in two-dimensional Fe_3GeTe_2 , *Nature* **563**, 94 (2018).
- [15] Y. Zhang, H. Lu, X. Zhu, S. Tan, W. Feng, Q. Liu, W. Zhang, Q. Chen, Y. Liu, X. Luo, D. Xie, L. Luo, Z. Zhang, and X. Lai, Emergence of kondo lattice behavior in a van der waals itinerant ferromagnet, Fe_3GeTe_2 , *Science Advances* **4**, eaao6791 (2018).
- [16] S. Bao, W. Wang, Y. Shangguan, Z. Cai, Z.-Y. Dong, Z. Huang, W. Si, Z. Ma, R. Kajimoto, K. Ikeuchi, S.-i. Yano, S.-L. Yu, X. Wan, J.-X. Li, and J. Wen, Neutron spectroscopy evidence on the dual nature of magnetic excitations in a van der waals metallic ferromagnet $\text{Fe}_{2.72}\text{GeTe}_2$, *Phys. Rev. X* **12**, 011022 (2022).
- [17] X. Wu, L. Lei, Q. Yin, N.-N. Zhao, M. Li, Z. Wang, Q. Liu, W. Song, H. Ma, P. Ding, Z. Cheng, K. Liu, H. Lei, and S. Wang, Direct observation of competition between charge order and itinerant ferromagnetism in the van der waals crystal $\text{Fe}_{5-x}\text{GeTe}_2$, *Phys. Rev. B*

- 104**, 165101 (2021).
- [18] X. Bai, F. Lechermann, Y. Liu, Y. Cheng, A. I. Kolesnikov, F. Ye, T. J. Williams, S. Chi, T. Hong, G. E. Granroth, A. F. May, and S. Calder, Antiferromagnetic fluctuations and orbital-selective mott transition in the van der waals ferromagnet $\text{Fe}_{3-x}\text{GeTe}_2$, *Phys. Rev. B* **106**, L180409 (2022).
- [19] X. Xu, Y. W. Li, S. R. Duan, S. L. Zhang, Y. J. Chen, L. Kang, A. J. Liang, C. Chen, W. Xia, Y. Xu, P. Malinowski, X. D. Xu, J. H. Chu, G. Li, Y. F. Guo, Z. K. Liu, L. X. Yang, and Y. L. Chen, Signature for non-Stoner ferromagnetism in the van der Waals ferromagnet Fe_3GeTe_2 , *Phys. Rev. B* **101**, 201104 (2020).
- [20] S. Bettler, F. Landolt, O. M. Aksoy, Z. Yan, S. Gvasaliya, Y. Qiu, E. Ressouche, K. Beauvois, S. Raymond, A. N. Ponomaryov, S. A. Zvyagin, and A. Zheludev, Magnetic structure and spin waves in the frustrated ferro-antiferromagnet $\text{Pb}_2\text{VO}(\text{PO}_4)_2$, *Phys. Rev. B* **99**, 184437 (2019).
- [21] V. K. Bhartiya, S. Hayashida, K. Y. Povarov, Z. Yan, Y. Qiu, S. Raymond, and A. Zheludev, Inelastic neutron scattering determination of the spin hamiltonian for $\text{BaCdVO}(\text{PO}_4)_2$, *Phys. Rev. B* **103**, 144402 (2021).
- [22] J. Pellicciari, S. Lee, K. Gilmore, J. Li, Y. Gu, A. Barbour, I. Jarrige, C. H. Ahn, F. J. Walker, and V. Bisogni, Tuning spin excitations in magnetic films by confinement, *Nature Materials* **20**, 188 (2021).
- [23] P. Abbamonte, G. Blumberg, A. Rusydi, A. Gozar, P. G. Evans, T. Siegrist, L. Venema, H. Eisaki, E. D. Isaacs, and G. A. Sawatzky, Crystallization of charge holes in the spin ladder of $\text{Sr}_{14}\text{Cu}_{24}\text{O}_{41}$, *Nature* **431**, 1078 (2004).
- [24] X. M. Chen, V. Thampy, C. Mazzoli, A. M. Barbour, H. Miao, G. D. Gu, Y. Cao, J. M. Tranquada, M. P. M. Dean, and S. B. Wilkins, Remarkable stability of charge density wave order in $\text{La}_{1.875}\text{Ba}_{0.125}\text{CuO}_4$, *Phys. Rev. Lett.* **117**, 167001 (2016).
- [25] Y. Shen, G. Fabbri, H. Miao, Y. Cao, D. Meyers, D. G. Mazzone, T. A. Assefa, X. M. Chen, K. Kisslinger, D. Prabhakaran, A. T. Boothroyd, J. M. Tranquada, W. Hu, A. M. Barbour, S. B. Wilkins, C. Mazzoli, I. K. Robinson, and M. P. M. Dean, Charge condensation and lattice coupling drives stripe formation in nickelates, *Phys. Rev. Lett.* **126**, 177601 (2021).
- [26] A. F. May, S. Calder, C. Cantoni, H. Cao, and M. A. McGuire, Magnetic structure and phase stability of the van der Waals bonded ferromagnet $\text{Fe}_{3-x}\text{GeTe}_2$, *Phys. Rev. B* **93**, 14411 (2016).

- [27] K. Yamagami, Y. Fujisawa, M. Pardo-Almanza, B. R. M. Smith, K. Sumida, Y. Takeda, and Y. Okada, Enhanced d-p hybridization intertwined with anomalous ground state formation in the van der Waals itinerant magnet Fe_5GeTe_2 , *Phys. Rev. B* **106**, 45137 (2022).
- [28] K. Yamagami, Y. Fujisawa, M. Pardo-Almanza, B. R. M. Smith, K. Sumida, Y. Takeda, and Y. Okada, Enhanced $d-p$ hybridization intertwined with anomalous ground state formation in the van der waals itinerant magnet fe_5gete_2 , *Phys. Rev. B* **106**, 045137 (2022).
- [29] A. Revelli, M. Moretti Sala, G. Monaco, C. Hickey, P. Becker, F. Freund, A. Jesche, P. Gegenwart, T. Eschmann, F. L. Buessen, S. Trebst, P. H. M. Van Loosdrecht, J. Van Den Brink, and M. Grüninger, Fingerprints of Kitaev physics in the magnetic excitations of honeycomb iridates, *Physical Review Research* **2**, 43094 (2020).
- [30] A. Revelli, M. Moretti Sala, G. Monaco, M. Magnaterra, J. Attig, L. Peterlini, T. Dey, A. A. Tsirlin, P. Gegenwart, T. Fröhlich, M. Braden, C. Grams, J. Hemberger, P. Becker, P. H. M. van Loosdrecht, D. I. Khomskii, J. van den Brink, M. Hermanns, and M. Grüninger, Quasimolecular electronic structure of the spin-liquid candidate $\text{Ba}_3\text{InIr}_2\text{O}_9$, *Phys. Rev. B* **106**, 155107 (2022).
- [31] K. Yamagami, Y. Fujisawa, B. Driesen, C. H. Hsu, K. Kawaguchi, H. Tanaka, T. Kondo, Y. Zhang, H. Wadati, K. Araki, T. Takeda, Y. Takeda, T. Muro, F. C. Chuang, Y. Niimi, K. Kuroda, M. Kobayashi, and Y. Okada, Itinerant ferromagnetism mediated by giant spin polarization of the metallic ligand band in the van der waals magnet fe_5Gete_2 , *Phys. Rev. B* **103**, L060403 (2021).
- [32] M. Silinskas, S. Senz, P. Gargiani, B. Kalkofen, I. Kostanovskiy, K. Mohseni, H. L. Meyerheim, S. S. P. Parkin, and A. Bedoya-Pinto, *Self-intercalation as origin of high-temperature ferromagnetism in epitaxially grown Fe_5GeTe_2 thin films* (2024), [arXiv:2309.17439 \[cond-mat.mtrl-sci\]](https://arxiv.org/abs/2309.17439).
- [33] Y. Gao, Q. Yin, Q. Wang, Z. Li, J. Cai, T. Zhao, H. Lei, S. Wang, Y. Zhang, and B. Shen, Spontaneous (anti)meron chains in the domain walls of van der waals ferromagnetic $\text{Fe}_{5-x}\text{GeTe}_2$, *Advanced Materials* **32**, 2005228 (2020).
- [34] S. Wu, R. Basak, W. Li, J.-W. Kim, P. J. Ryan, D. Lu, M. Hashimoto, C. Nelson, R. Acevedo-Esteves, S. C. Haley, J. G. Analytis, Y. He, A. Frano, and R. J. Birgeneau, Discovery of charge order in the transition metal dichalcogenide fe_xnbs_2 , *Phys. Rev. Lett.* **131**, 186701 (2023).
- [35] S. E. Brown, E. Fradkin, and S. A. Kivelson, Surface pinning of fluctuating charge order: An extraordinary surface phase transition, *Phys. Rev. B* **71**, 224512 (2005).

- [36] Q. Gu, J. P. Carroll, S. Wang, S. Ran, C. Broyles, H. Siddiquee, N. P. Butch, S. R. Saha, J. Paglione, J. C. S. Davis, and X. Liu, Detection of a pair density wave state in UTe_2 , *Nature* **618**, 921 (2023).
- [37] C. S. Kengle, J. Vonka, S. Francoual, J. Chang, P. Abbamonte, M. Janoschek, P. F. S. Rosa, and W. Simeth, Absence of bulk charge density wave order in the normal state of UTe_2 (2024), [arXiv:2406.14690 \[cond-mat.str-el\]](https://arxiv.org/abs/2406.14690).
- [38] F. Theuss, A. Shragai, G. Grissonnanche, L. Peralta, G. de la Fuente Simarro, I. M. Hayes, S. R. Saha, Y. S. Eo, A. Suarez, A. C. Salinas, G. Pokharel, S. D. Wilson, N. P. Butch, J. Paglione, and B. J. Ramshaw, Absence of a bulk thermodynamic phase transition to a density wave phase in UTe_2 (2024), [arXiv:2406.14714 \[cond-mat.str-el\]](https://arxiv.org/abs/2406.14714).
- [39] J. Mayer, L. A. Giannuzzi, T. Kamino, and J. Michael, TEM Sample Preparation and FIB-Induced Damage, *MRS BULLETIN* **32**, 401 (2007).
- [40] C. A. Volkert and A. M. Minor, Focused ion beam microscopy and micromachining, *MRS Bulletin* **32**, 389 (2007).
- [41] J. Dvorak, I. Jarrige, V. Bisogni, S. Coburn, and W. Leonhardt, Towards 10 meV resolution: The design of an ultrahigh resolution soft X-ray RIXS spectrometer, *Review of Scientific Instruments* **87** (2016).
- [42] K. Momma and F. Izumi, *VESTA*: a three-dimensional visualization system for electronic and structural analysis, *Journal of Applied Crystallography* **41**, 653 (2008).

FIGURES

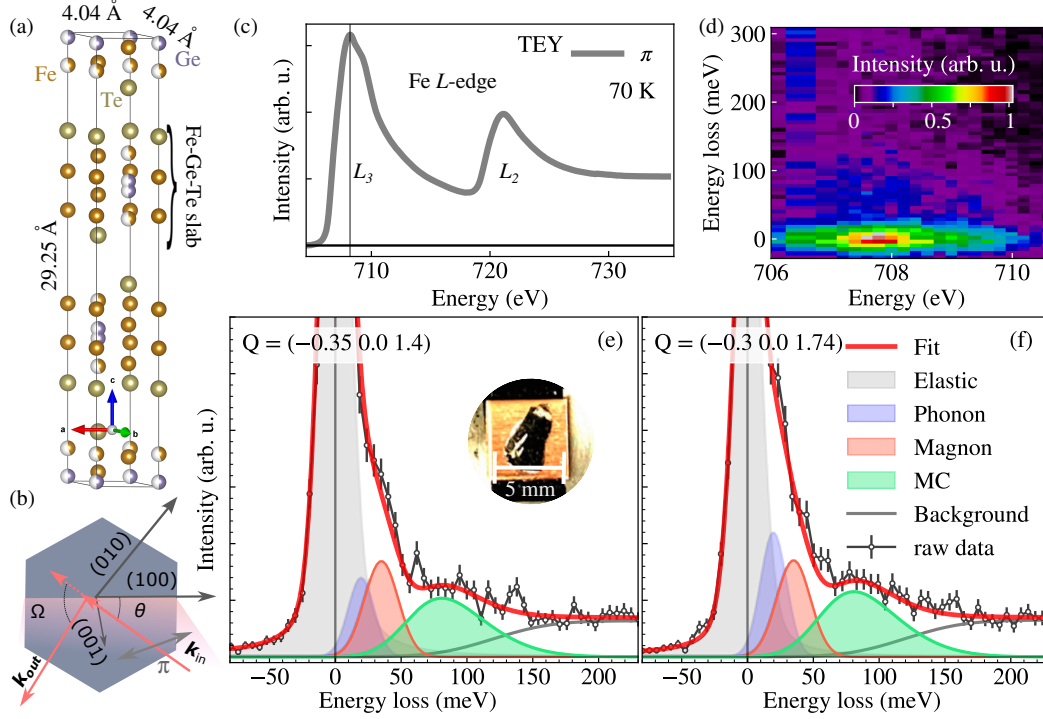


FIG. 1. Magnetic excitations in the Fe L_3 -edge RIXS spectra of Fe_5GeTe_2 . (a) Fe_5GeTe_2 crystal structure drawn using VESTA [42]. A single unit cell contains three Fe-Ge-Te slabs. (b) Schematic of RIXS experimental geometry. In the hexagonal structure representation, two orthogonal wave vectors – (100) and (001) – form the scattering plane highlighted in pink. θ is an angle between the incident x-ray and the (100) axis while Ω is the scattering angle between incoming and outgoing x-ray. The double headed arrow represents the π polarization of the incident light. (c) Fe $L_{3,2}$ -edge XAS measured at $\theta = 15^\circ$ in total electron yield (TEY) mode at 70 K. A solid vertical line represents the Fe L_3 -edge maximum, that corresponds to the incident photon energy (707.9 eV) used for the RIXS spectra. (d) RIXS intensity map measured as a function of incident photon around the Fe L_3 -edge, and zoomed in to cover excitations below 300 meV. For this dataset, $\theta = 20^\circ$ and $\Omega = 95^\circ$ corresponding to $\mathbf{Q} = (-0.16 \ 0 \ 2.17)$. (e-f). Two representative RIXS scans (black dotted line) at $(-0.35 \ 0 \ 1.4)$ and $(-0.3 \ 0 \ 1.74)$. The low-energy excitations are fitted with an elastic peak (gray), a phonon (blue), a magnon (red), a broad continuum, and a background (gray line) stretching to higher energies. The red solid line represents the fit sum. The inset in (e) shows the measured Fe_5GeTe_2 single crystal. All RIXS spectra displayed in this work were measured at $T = 70$ K, using π polarization. The error bars of the RIXS spectra are defined assuming a Poisson distribution of the single-photon counted events.

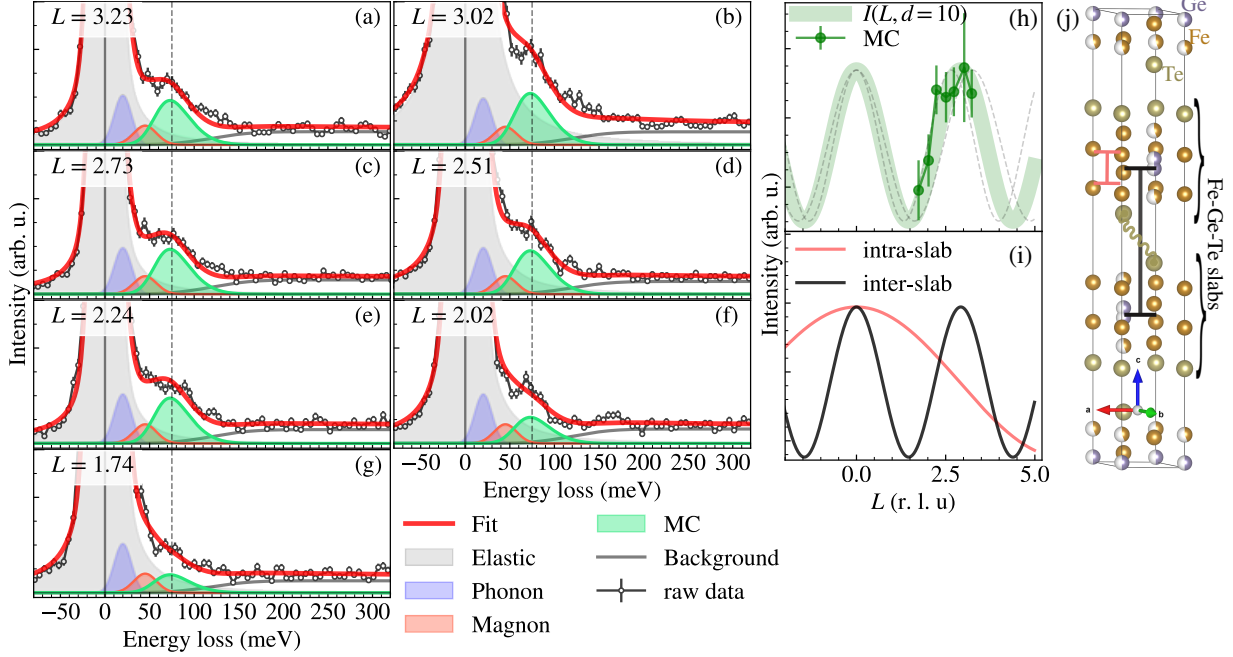


FIG. 2. L – dependent study of the magnetic continuum in Fe_5GeTe_2 . (a-g) RIXS spectra measured at different L values from 1.74 r.l.u. to 3.23 r.l.u., at 70 K. For all spectra, $H < |0.04|$ and $K = 0$. Each spectrum is fitted with an elastic peak (gray), a phonon (blue), a magnon (red), and a continuum (green), as introduced in Figs. 1(e, f). The vertical dashed line marks the continuum centers around ~ 75 meV. (h) L -dependence of the continuum integrated spectral weight (green dotted line). The error-bars are extracted from the fitting through the error propagation method. The thick green line is a sinusoidal fit of the data using Eq. (1) for $d = 10$ Å, while the dotted lines represent the upper and lower boundaries considering the extracted fit error for d of ± 1 Å. (i) Calculated intensity modulation for intra-slab (red) and inter-slab (black) distances, as defined within the crystal structure displayed in (j) using with the same color convention. A gold curved line in (j) highlights the Te – Te distance across two neighboring slabs.

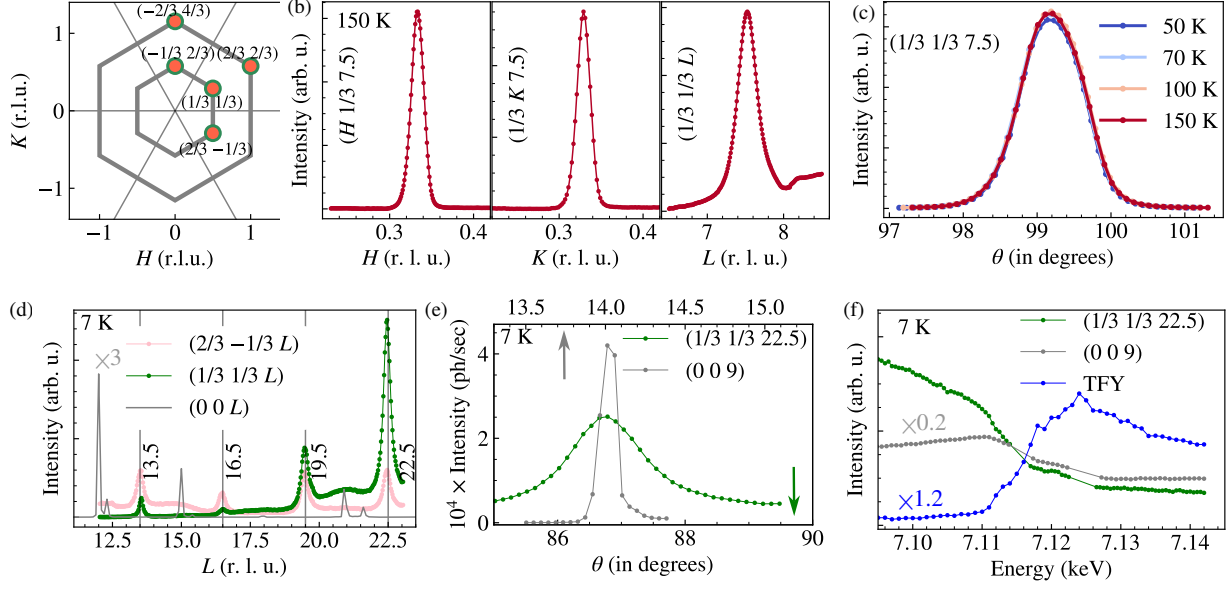


FIG. 3. Investigation of charge order in Fe_5GeTe_2 by REXS and XRD. (a) A sketch highlighting the measured symmetry equivalent Q positions. (b) H , K , and L scans of a representative $(1/3, 1/3, 7.5)$ peak using 2.1 keV x-ray energy at 150 K. (c) The temperature dependence of the $(1/3, 1/3, 7.5)$ peak. (d) Fixed-energy Q -scan of $(1/3, 1/3, L)$ (green dotted line), $(2/3, -1/3, L)$ (pink dotted line), and of $(0, 0, L)$ (gray line) along the L direction. The temperature was set to 7 K for this measurement and the x-ray energy was tuned prior to the Fe K -edge, ~ 7.1 keV. Double peaks in $(0, 0, L)$ scan are due to a second crystallite. $(0, 0, L)$ scan is rescaled to match y-scale. (e) Absolute intensity comparison between $(1/3, 1/3, 22.5)$ and $(0, 0, 9)$ peaks. (f) Fixed- Q energy scan of $(1/3, 1/3, 22.5)$ (green dotted line) and $(0, 0, 9)$ (gray dotted line) peaks, rescaled to match y-scale. The Fe K -edge XAS of Fe_5GeTe_2 measured in total fluorescence yield (TFY) mode is displayed (rescaled) for reference (blue dotted line).

1 **Supplementary information for “Investigation of magnetic**
 2 **excitations and charge order in a van der Waals ferromagnet**
 3 **Fe₅GeTe₂ ”**

4 V. K. Bhartiya,^{1,*} T. Kim,¹ J. Li,¹ T. P. Darlington,² D. J. Rizzo,²
 5 Y. Gu,¹ S. Fan,¹ C. Nelson,¹ J. W. Freeland,³ X. Xu,⁴ D. N.
 6 Basov,² J. Pelliciani,¹ A. F. May,⁵ C. Mazzoli,¹ and V. Bisogni^{1,†}

7 ¹*National Synchrotron Light Source II, Brookhaven*
 8 *National Laboratory, Upton, New York 11973, USA.*

9 ²*Department of Physics, Columbia University, New York, New York 10027, USA.*

10 ³*Advanced Photon Source, Argonne National Laboratory, Lemont, IL, USA.*

11 ⁴*Department of Physics, University of Washington, Seattle, Washington 98195, USA.*

12 ⁵*Materials Science and Technology Division,*
 13 *Oak Ridge National Laboratory, Oak Ridge, Tennessee 37831, USA.*

14 **CONTENTS**

15	S1. Phonons	2
16	S2. Self-absorption correction to the RIXS intensity	2
17	S3. RIXS spectrum fitting procedure	3
18	References	4

* vbhartiya1@bnl.gov

† bisogni@bnl.gov

19 **S1. PHONONS**

20 We performed room-temperature Raman scattering ($\lambda = 6328 \text{ \AA}$) on the exfoliated flake
 21 (oriented as c -axis normal) to determine phonons in Fe_5GeTe_2 , see Fig. S1.1. For these
 22 measurements, we exfoliated a Fe_5GeTe_2 flake on SiO_2/Si . The strongest phonon is observed
 23 below $< 150 \text{ cm}^{-1}$ (20 meV) i.e. no overlap with magnon or continuum. We assume 20 meV
 24 phonon to have the dominant contribution in the resonant inelastic X-ray scattering (RIXS)
 25 spectrum. Raman lines around 62 meV originates from Si/SiO_2 substrate.

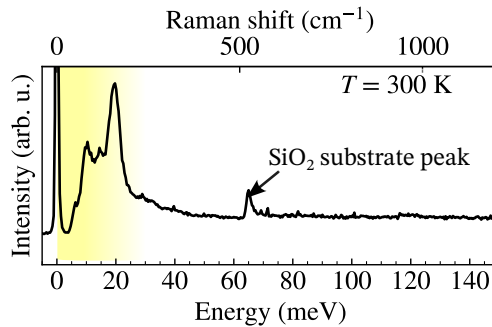


FIG. S1.1. Raman scattering from an exfoliated flake. The contribution from phonons to the
 26 spectrum is $\leq 20 \text{ meV}$, highlighted by yellow color region.

27

28 **S2. SELF-ABSORPTION CORRECTION TO THE RIXS INTENSITY**

29 Outgoing photons with energy close to the absorption/resonance edge get considerably
 30 reabsorbed. Moreover, the path length traveled or the time spent by the photons inside
 31 the sample depends on the scattering geometry. Both effects combined affect the measured
 32 RIXS intensity, and when comparing absolute signal of two or more scattering geometries,
 33 it is essential to consider these aspects. The raw RIXS intensity can be corrected, to the
 34 first approximation, for these effects with information of X-ray absorption measured in total
 35 electron yield (TEY) and the corresponding scattering geometry [1]. RIXS data shown in
 36 the main body of the paper was corrected for self-absorption effects following the procedure
 37 used in Refs. [1, 2]. Only scattering geometry lead self-absorption effects are considered as
 38 no dichroism is observed in TEY – similar absorption profile for σ and π - polarizations. The
 39 corrected RIXS intensity I_c is given as following:

$$I_c = I_m \otimes \mathcal{A}(\theta, \Omega, \mu(\omega_{in}), \mu(\omega_{out})) \quad (1)$$

40 where I_m is measured RIXS intensity and the self-absorption correcting factor \mathcal{A} is defined
41 as,

$$\mathcal{A} = \frac{\mu(\omega_{in}) \sin(\Omega - \theta) + \mu(\omega_{out}) \sin \theta}{\sin(\Omega - \theta)} \quad (2)$$

42 \mathcal{A} is a function of scattering geometry (Ω is angle between incoming and outgoing photon
43 and θ is photon incidence angle measured from the sample surface as shown in Fig. 1(a),
44 TEY, and, incoming and outgoing photon energy, $\mu(\omega_{in})$ is the total electron-yield (TEY)
45 maximum (at Fe L_3 - resonance) and $\mu(\omega_{out})$ is TEY value at the corresponding ω_{out} . TEY
46 was measured in the same ($\theta - \Omega$) scattering geometry as RIXS.

47 S3. RIXS SPECTRUM FITTING PROCEDURE

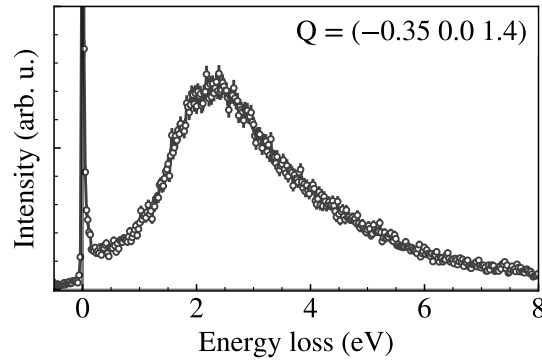


FIG. S3.1. A representative raw RIXS spectrum. The florescence peak around 2 eV is a signature of metallic system. Its low energy part containing magnetic excitation (shown in Fig. 1(e)) is used for modeling.

48 In this section we describe the fitting procedure of the self-absorption corrected low-
49 energy portion [0 – 300] meV RIXS intensity. A complete RIXS scan is shown in Fig. S3.1.
50 The elastic line was modeled by a Pseudo-Voigt model:

$$f_1(x; A, \mu, \sigma, \alpha) = \frac{(1 - \alpha)A}{\sigma_g \sqrt{2\pi}} e^{-(x-\mu)^2/2\sigma_g^2} + \frac{\alpha A}{\pi} \frac{\sigma}{(x - \mu)^2 + \sigma^2} \quad (3)$$

51 and the phonon and magnon by a Gaussian distribution:

$$f_2(x; A, \mu, \sigma) = \frac{A}{\sigma\sqrt{2\pi}} e^{[-(x-\mu)^2/2\sigma^2]} \quad (4)$$

52 while to accommodate the damped and broad character of the continuum, it was modeled
53 by a Skewed Gaussian:

$$f_3(x; A, \mu, \sigma, \gamma) = \frac{A}{\sigma\sqrt{2\pi}} e^{[-(x-\mu)^2/2\sigma^2]} \left\{ 1 + \operatorname{erf}\left[\frac{\gamma(x-\mu)}{\sigma\sqrt{2}}\right] \right\} \quad (5)$$

54 The fluorescence tail background was modeled by a step function broadened by the twice
55 experimental resolution:

$$f_4(x, A_0, A, \mu, \sigma) = A[1 + \operatorname{erf}((x-\mu)/\sigma)]/2 \quad (6)$$

56 Here A is the amplitude, μ is the center, σ is the standard-deviation, α is the fraction,
57 Final model describing the entire RIXS spectrum for $E < 300$ meV. As a result, function
58 capturing the low energy RIXS spectrum is as follows –

$$I = \text{Elastic}(f_1) + \text{Phonon}(f_2) + \text{Magnon}(f_2) \\ + \text{Continuum}(f_3) + \text{Background}(f_4) \quad (7)$$

59

60

61 During fitting of all the RIXS spectra vs Q , the following procedure was adopted. Elastic
62 line: σ, α was kept fixed and only amplitude A and μ were allowed to change. σ was fixed
63 by the experimental resolution. Phonon: σ was fixed by experimental resolution and μ was
64 fixed to 20 meV from the Raman measurements and amplitude A was allowed to change as
65 $\sin^2(\pi L)$ [3] for in-plane scans, however, it was fixed for out-of-plane dependence. Magnon:
66 Both A and μ were allowed to change, but σ was fixed to a higher value than the resolution
67 to account for continuum contamination, for out-of-plane scans, both A and μ were fixed.
68 Continuum: Both its position μ and width σ and γ were fixed, however, its amplitude A
69 was allowed to change. Background amplitude A was fixed to mean ($200 < I < 450$).

70 [1] R.-P. Wang, H. Elnaggar, C. J. Titus, K. Tomiyasu, J. Geessinck, G. Koster, F. Frati,
71 J. Okamoto, D.-J. Huang, and F. M. F. De Groot, Saturation and self-absorption effects in

- 72 the angle-dependent 2p3d resonant inelastic X-ray scattering spectra of Co^{3+} , *J. Synchrotron*
73 *Rad* **27**, 979 (2020).
- 74 [2] H. C. Robarts, M. García-Fernández, J. Li, A. Nag, A. C. Walters, N. E. Headings, S. M.
75 Hayden, and K.-J. Zhou, Dynamical spin susceptibility in La_2CuO_4 studied by resonant inelastic
76 x-ray scattering, *Phys. Rev. B* **103**, 224427 (2021).
- 77 [3] J. Q. Lin, H. Miao, D. G. Mazzone, G. D. Gu, A. Nag, A. C. Walters, M. García-Fernández,
78 A. Barbour, J. Pelliciani, I. Jarrige, M. Oda, K. Kurosawa, N. Momono, K.-J. Zhou, V. Bisogni,
79 X. Liu, and M. P. M. Dean, Strongly correlated charge density wave in $\text{La}_{2-x}\text{Sr}_x\text{CuO}_4$ evidenced
80 by doping-dependent phonon anomaly, *Phys. Rev. Lett.* **124**, 207005 (2020).